



**HAL**  
open science

# On modeling the dynamic response induced by fracturing brittle materials

Dac Thuong Ngo, Frederic L Pellet

## ► To cite this version:

Dac Thuong Ngo, Frederic L Pellet. On modeling the dynamic response induced by fracturing brittle materials. *Engineering Fracture Mechanics*, 2020, 224, pp.106802 -. 10.1016/j.engfracmech.2019.106802 . hal-03488428

**HAL Id: hal-03488428**

**<https://hal.science/hal-03488428>**

Submitted on 7 Mar 2022

**HAL** is a multi-disciplinary open access archive for the deposit and dissemination of scientific research documents, whether they are published or not. The documents may come from teaching and research institutions in France or abroad, or from public or private research centers.

L'archive ouverte pluridisciplinaire **HAL**, est destinée au dépôt et à la diffusion de documents scientifiques de niveau recherche, publiés ou non, émanant des établissements d'enseignement et de recherche français ou étrangers, des laboratoires publics ou privés.



Distributed under a Creative Commons Attribution - NonCommercial 4.0 International License

## On modeling the dynamic response induced by fracturing brittle materials

Dac Thuong NGO<sup>1</sup>, Frederic L. PELLET<sup>1,2</sup>

<sup>1</sup>Mines ParisTech – PSL University, Center for Geosciences and Geo-Engineering, Fontainebleau, FRANCE

<sup>2</sup>INSA University of Lyon – Department of Mechanical Engineering - Villeurbanne, FRANCE

### Abstract:

A comprehensive approach is developed to model the dynamic effects induced by fracturing brittle materials through quasi-static loadings. This involves the establishment of a rigorous 1D analytical model to answer, in a quantitative way, the question of how elastic waves can be induced by the damage of the material. By analyzing the conversion of strain energy into kinetic energy, it is found that the rate of fracture opening is driven by a factor that depends on the fracture tensile strength, the fracture toughness and the Young's modulus of the material. Dynamic Finite Element Analysis is then performed to determine the most sensitive parameters. It is found that the velocities of induced elastic waves are insensitive to the loading rate but increase substantially when the tensile strength of the material increases. This finding is of interest for many rock engineering problems, for instance the assessment of induced micro-seismicity triggered during geothermal energy extraction.

### 1 Introduction

Fracturing brittle materials leads to a dynamic response that can occur even if the loading is quasi-static. This phenomenon has been widely studied (Rosakis and Ravichandran, 2000; Ravi-Chandar, 2004; Petrov et al., 2016) and observed, particularly during testing of rock-like materials where the Acoustic Emissions (AE) have been recorded. In many rock engineering situations, the process of rock fracturing can induce micro-seismicity, for instance in rock bursting in deep underground mines or during hydraulic stimulation of deep geothermal

reservoirs, (Ngo et al., 2019). However, to date there is still no comprehensive approach to model the phenomenon of induced dynamic effects related to rock fracturing.

In the following sections, a rigorous 1D analytical model is presented to quantitatively address the question of how elastic waves are generated when the strain energy stored in a body leads to material damage and dynamic fracturing. This study first considers the tensile mode of rupture (Mode I) and then a dynamic Finite Element Analysis is performed using the Cohesive Zone Model to validate the results obtained from the analytical model.

## **2 Previous studies on the dynamic response induced by fracturing**

### **2.1 Experimental evidence**

Numerous experimental studies on brittle materials have shown that their failure is reflected in the initiation and propagation of fractures that generate elastic waves. At a laboratory scale, Acoustic Emissions (AE) are recorded ( Swindlehurst, 1973; Ohnaka and Mogi, 1982; Hardy Jr, 2003) whereas on a larger scale the induced micro-seismicity (MS) is measured (Scholz, 1968a, b; Evans and Linzer, 1977; Lockner, 1993).

One explanation for this wave generation can be found through a micro-structural analysis of the material. Indeed, it appears that the sudden breakage of atomic bonds allows a fracture to form and propagate (Keshavarz et al., 2008; Moradian et al., 2016); the resulting elastic waves can be recorded by AE/MS sensors, as shown in Figure 1 .

During the fracturing process, the energy balance of the system is changed: part of the stored strain energy that is not consumed to create fractures is converted into kinetic energy in the form of elastic waves that will propagate within the medium (Pellet and Selvadurai, 2016).

Figure 1 (a) Illustration of generation of elastic waves from fracture propagation, (b) Example of signals recorded by AE/MS sensors (e.g., acceleration)

## 2.2 Most common numerical approaches

There are currently three main numerical methods used as modeling techniques for the dynamic fracturing process: the conventional or the extended finite element method (FEM-XFEM), the discrete element method (DEM) and the combined finite-discrete element method (FDEM).

In the finite element method, the fracturing process is modeled using damage mechanics (Tang, 1997; Kaiser and Tang, 1998; Tang and Kaiser, 1998). The material is modeled according to the damage constitutive law and AE/MS are simulated based on the assumption that the number of induced dynamic events is proportional to the number of elements that are damaged. The strain energy released in the damaged elements is considered to be analogous to the AE/MS energy.

As an example, we show below the results of a XFEM numerical modeling of a Brazilian test (Indirect Tensile Test) performed on a granite specimen (Keshavarz et al., 2008). Complete data can be found in Ngo et al. (2017). Figure 2 shows a good agreement between the computed load-displacement curve and the experimental one (Figure 2a), whereas the crack propagation and the subsequent stress redistribution is displayed in Figure 2b. The computed velocity at point M versus time is reported in Figure 2c.

It has to be pointed out that in lab experiments, most of the observation are based on Acoustic Emission records. Because of the use of piezo electric sensors, the collected data are expressed in voltage and there is no direct relationship to transform the electrical signal in velocity [ $\text{m}\cdot\text{s}^{-1}$ ] or acceleration [ $\text{m}\cdot\text{s}^{-2}$ ]. Therefore, only qualitative comparisons are possible.

Figure 2: Numerical simulation of a Brazilian test (Ngo et al. 2017); a- load-displacement curve; b- fracture propagation and stress redistribution, c- acceleration versus time in point M

In discrete element models, the material is represented as an assembly of particles that have the shape of a circular disc for 2D models or a sphere for 3D models (Cundall and Hart, 1992; Potyondy and Cundall, 2004). These particles are bonded together and interact with each other at contact points where constitutive contact laws are required to describe their normal and shear interactions. When the shear or tensile stress exceeds the shear or tensile strength of a

contact bond, the latter is broken allowing a crack to initiate and propagate. The magnitude of an induced dynamic event is calculated based on the change in kinetic energy of particles before and after one or several bonds are broken. The method was used by Hazzard and Young (2000, 2004) to simulate triaxial compression tests and a mine-by tunnel experiment. The authors showed that the model was able to reproduce the Gutenberg-Richter relationship (Gutenberg and Richter, 1956) which expresses the seismic magnitude as a function of the number of induced dynamic events. More specifically, they were able to obtain the numerical  $b$ -value within the range obtained from experiments.

In the combined finite-discrete element method, the intact material is typically assumed to be linear elastic and is modeled by finite elements. Cohesive elements are then inserted between the finite elements to model the fracture initiation and propagation (Munjiza, 2004). Once the fracture has occurred, the blocks of material created are treated as discrete blocks. The kinetic energy that is induced by the fracture propagation is considered to be the AE/MS energy. This method was used by Lisjak et al. (2013) to simulate the induced dynamic effects in an unconfined compression test on granite. The authors reported that the magnitude of the simulated event tended to display as a power-law distribution, with  $b$  values in agreement with those reported in the literature for granitic rocks.

The three numerical methods briefly presented above have had some success in reproducing several features of the dynamic effects induced by fracture propagation (e.g.,  $b$ -value in the range found in experiments). However, the following fundamental questions (FQ) have not yet been fully resolved:

- FQ1: How can dynamic response ~~effects~~ be generated through fracture propagation, even when the loading is quasi-static?
- FQ2: How much of the stored strain energy is converted into kinetic energy in the form of elastic waves?
- FQ3: What parameters have the greatest influence on the induced dynamic response ~~effects~~?

Several text books attempt to address this and Some research provides partial answers to these fundamental questions. For question FQ1, Keshavarz et al. (2008) and Moradian et al. (2016) showed, by testing brittle rocks and recording the AEs, that fracture propagation can induce dynamic response—effects—even when the loading rate is quasi-static. For question FQ2, Kanamori (1977) proposed that a fraction ( $2 \times 10^{-5}$ ) of the strain energy change is converted into the kinetic energy of induced elastic waves. For the question FQ3, several authors (Fineberg et al., 1992; Boudet et al., 1995; Batrov and Petrov, 2007) suspected that there was some relationship between the velocity of fracture propagation or the fault slip rate and the intensity of the induced dynamic effects. These explanations are plausible but they still do not address the above questions in a quantitative way. Therefore, in the following section quantitative answers to these fundamental questions are proposed.

### **3 Discrete models for generating a dynamic response through damage**

In this section, an existing discrete model that provides an indication of how dynamic effects can be induced through material damage is presented. Then an extension of the discrete model is proposed to more clearly illustrate this phenomenon.

#### **3.1 Pollock's model**

From the energy balance point of view, the generation of elastic waves from fracturing material is a process of conversion of strain energy into kinetic energy. A physics-based approach to modeling induced elastic waves must be able to model this energy conversion process. To our knowledge, the only model that illustratively explains the conversion of strain energy into kinetic energy was proposed by Pollock (1973). The model consists of a mass  $m$  suspended by two springs of stiffness  $K$  (Figure 3). The stiffness of the lower spring is assumed to instantaneously change by an amount  $\delta K$ . As the stiffness of the system is suddenly changed, the mass will move toward and vibrate around a new equilibrium position. The change in strain energy due to the decrease of stiffness of the system  $\Delta E_s$  and the peak kinetic energy of the mass  $E_{kin}$  are, according to Pollock (1973) , expressed as followed:

$$\Delta E_s = \frac{1}{8} \delta K \cdot x^2 \quad ; \quad E_{kin} = \frac{1}{8} \frac{(\delta K)^2}{K} x^2 \quad (1)$$

where  $x$  is initial extension of the spring system

From equation (1), the ratio between the kinetic energy and the change in strain energy is obtained as  $\Delta E_s / E_{kin} = \delta K / K$ .

Figure 3 A spring-mass model after Pollock (1973)

Thus, Pollock's model shows that the amount of induced kinetic energy is proportional to the change in the stiffness of the system. For a continuum material, the stiffness change can originate from the propagation of fracture and the resulting damage.

### 3.2 New discrete model

To more clearly illustrate the generation of dynamic response ~~effects~~ from the damage, regardless of the loading rate, we also use a spring-mass model as shown in Figure 4. The model consists of two masses  $M_1$  and  $M_2$ , and two springs 1 and 2. Each spring is characterized by its stiffness and its tensile strength:  $K_1$  and  $R_1$  for spring 1,  $K_2$  and  $R_2$  for spring 2. Let us assume that the tensile force  $R_2$  is smaller than  $R_1$  ( $R_2 < R_1$ ).

When the system is loaded by controlling the displacement of the mass  $M_2$  (as illustrated in Figure 4) the latter is pulled downwards and internal forces of the same magnitude are generated in both of the springs. At some point the internal force reaches the tensile strength of spring 2,  $R_2$ , and spring 2 breaks. Let us assume that the failure of the spring 2 is instantaneous; when spring 2 fails the mass  $M_1$ , which has been displaced from its initial position to a distance  $a$ , is free to move. The movement of the mass  $M_1$  after spring 2 has broken is a harmonic vibration with the following characteristics:

- Displacement of M1:  $x = a \cos(\omega t)$  (2)

- Velocity of M1:  $v = -\omega a \sin(\omega t)$  (3)

- Kinetic of M1:  $E_k = \frac{1}{2} m_1 v^2 = \frac{1}{4} K_1 a^2 [1 - \cos(2\omega t)]$  (4)

- Strain energy of spring 1:  $E_s = \frac{1}{2} K_2 x^2 = \frac{1}{4} K_2 a^2 [1 + \cos(2\omega t)]$  (5)

where  $\omega$  is the angular frequency; and  $a$  is the displacement of the mass M1 when spring 2 breaks and is equal to  $R_2/K_1$ .

Thus, the maximum kinetic energy  $E_{kmax}$  of the mass M1 is:

$$E_{kmax} = \frac{1}{2} K_1 a^2 = \frac{1}{2} \frac{R_2^2}{K_1} \quad (6)$$

The time evolution of the kinetic and the strain energies is presented in Figure 5. From equations (2) to (6) and Figure 5, the followings comments can be made:

- (i) The kinetic energy of the mass M1 is proportional to the tensile strength of the spring 2 and is inversely proportional to the stiffness of the spring 1 (equation (6))
- (ii) There is a conversion between kinetic and strain energy: when the kinetic energy is zero the strain energy is maximum, and vice versa (Figure 5)
- (iii) The frequency of kinetic energy and strain energy is twice the frequency of the displacement or the velocity (equations (2) to (5) and Figure 5)

Figure 4 Proposed spring-mass model: K1 and R1 are the stiffness and strength of spring 1, K2 and R2 are the stiffness and strength of spring 2

Figure 5 Time evolution of kinetic energy and strain energy;  $T$  is the period of the vibration of the mass

M1

In the calculations, the strain energy of the spring 2 and the energy loss due to the breakdown of spring 2 are not included. For a discrete system of springs and masses, these simplifications are acceptable. The calculation clearly shows that the intensity of the induced dynamic effects, which is reflected by the maximum kinetic energy, depends on two factors: the strength and the stiffness of the system. It should also be noted that the kinetic energy of the mass M1 is shown to be independent of the rate of the applied displacement. This means that no matter how slowly the displacement is applied, the mass M1 will vibrate harmonically once the spring 2 is broken and maximum kinetic energy of the mass M1 remains the same. By using this simple spring-mass model, the questions FQ1 and FQ3 are clearly and quantitatively addressed.

#### 4 Continuum model

To extend the previous conclusion to a continuum model, a plate subjected to an uniaxial tension is modeled in order to show that elastic waves can be induced even when the loading rate is quasi-static. The unit width of the plate under study, whose height is  $L$ , is composed of two parts as shown in Figure 6.

The fracture (upper part) is a zero-thickness layer, modeled using the Cohesive Zone Model whose constitutive law is characterized by the tensile strength  $R_T$  and fracture toughness  $G_{IC}$  (Figure 7). The other part of the plate consists of a linear elastic material, which is characterized by a Young's modulus  $E$  and a Poisson's ratio  $\nu$ . The loading is applied by controlling the displacement rate of the top edge of the plate (Figure 6). As the applied displacement increases, the cohesive layer will be damaged and the separation rate of the cohesive layer is calculated. In this subsection, only the phase after the onset of damage to the cohesive layer is considered (i.e., after the stress in the cohesive layer has reached the tensile strength and after the two faces of the cohesive layer start to separate).

Figure 6 Plate model made of two materials. The cohesive layer has zero thickness.

Figure 7: Cohesive traction-separation law

For each stress increment in the cohesive layer  $\Delta\sigma$  ( $\Delta\sigma < 0$ ), the corresponding displacement increment of top edge of the plate  $\Delta u$  consists of 2 components:

$$\Delta u = \Delta u_c + \Delta u_s \quad (7)$$

where  $\Delta u_c$  is the separation increment of the cohesive layer and  $\Delta u_s$  is the change in length of the elastic part.  $\Delta u_c$  and  $\Delta u_s$  are determined by:

$$\begin{aligned} \Delta u_c &= \frac{\Delta\sigma}{K(u_c)} \\ \Delta u_s &= \frac{\Delta\sigma}{E} L \end{aligned} \quad (8)$$

where  $K(u_c)$  is the slope of the cohesive traction – separation curve (Figure 7), which is  $-R_T / \delta_f$ .

Combining equations (7) and (8) leads to:

$$\Delta u_c = \frac{1}{1 - \frac{R_T}{E} \frac{L}{\delta_f}} \Delta u \quad (9)$$

Dividing both sides of equation (9) by  $\Delta t$  - the time increment during which the stress increment  $\Delta\sigma$  takes place - gives:

$$\dot{u}_c = \frac{1}{1 - \frac{R_T L}{E \delta_f}} \dot{u} \quad (10)$$

Since  $G_{IC} = 0.5R_T \delta_f$ , equation (9) can be rewritten as:

$$\dot{u}_c = \frac{1}{1 - \frac{R_T^2 L}{2G_{IC} E}} \dot{u} \quad (11)$$

In equation (11),  $\dot{u}_c$  and  $\dot{u}$  are the separation rate of the cohesive layer and the applied displacement rate, respectively.

Let us denote  $\alpha$  as:

$$\alpha = \frac{R_T^2 L}{2G_{IC} E} \quad (12)$$

Then, equation (11) becomes:

$$\dot{u}_c = \frac{1}{1 - \alpha} \dot{u} \quad (13)$$

From equation (13), we observe that as the factor  $\alpha \rightarrow 1$  the separation rate of the cohesive layer  $\dot{u}_c$  becomes very large regardless of the applied displacement rate. This large separation rate of the cohesive layer means that elastic waves are generated.

It can also be seen that if the length of the plate is large enough,  $\alpha$  can be larger than 1. In such cases  $\dot{u}_c$  will become negative. However, as the displacement continues to increase after damage initiation of the cohesive layer has occurred, the separation of the cohesive layer will increase with time and thus  $\dot{u}_c$  must be positive.

This leads to the conclusion that in cases where  $\alpha > 1$ , the calculation above is no longer valid. In fact, in the above calculation it is assumed that when the stress in the cohesive layer is changed by an increment  $\Delta\sigma$ , the whole plate experiences the same stress increment  $\Delta\sigma$ . This is indeed the case as long as  $\alpha < 1$ . When  $\alpha > 1$ , if the stress in the cohesive layer is changed by  $\Delta\sigma$ , this stress change will not affect the whole plate instantaneously. Instead, the stress change will "propagate" as elastic stress waves from the region close to the cohesive layer to outlying regions without dependence on the applied displacement rate. The length  $L$  of the plate can be seen as a characteristic length of the material. A closer look shows that  $\alpha$  is in fact the ratio between the change in strain energy before damage initiation,  $R_T^2 L / (2E)$ , and the energy loss due to fracture  $G_{IC}$ .

In conclusion, if the strain energy that is released during fracture development is larger than the energy needed to create a new fracture surface (i.e., the fracture energy), elastic waves will be generated regardless of the loading rate. The amplitude of the induced elastic waves is proportional to the ratio between the strain energy release and the fracture energy.

## 5 Numerical modeling

The model presented in section 4 is now numerically investigated using the Finite Element Method (Abaqus, 2016). Here again, the objective is to model the elastic waves induced by the fracture and to identify the factors likely to influence their amplitude. The following points have to be demonstrated:

- (i) Elastic waves are induced if  $\alpha$ , (i.e., the ratio between the change in strain energy  $E_S$  before and after fracture occurs and the energy loss due to the fracture  $E_F$ ) is larger than 1 (to be studied in subsection 5.1)
- (ii) The loading rate does not affect the induced elastic waves (to be studied in subsection 5.2)
- (iii) The amplitude of the induced elastic waves are also augmented if  $\alpha$  increases (to be studied in subsection 5.3)

## 5.1 Induced elastic wave simulation when $\alpha > 1$

### 5.1.1 Model set up

The plate under studied has a width  $W = 0.2$  m and a length  $L = 1$  m. The top edge of the plate is pulled upwards at a constant and relatively small rate, such that the loading does not introduce any dynamic effect. In this simulation, a displacement rate of 9 mm/s, which corresponds to a strain rate  $9 \cdot 10^{-3} \text{ s}^{-1}$ , is chosen. An illustration of the model with the boundary conditions and the loading is given in Figure 8. With these boundary and loading conditions, the problem is equivalent to a 1D problem and, therefore, only the displacement, velocity, and acceleration in direction 2 are non-zero. Thus, the words displacement, velocity, and acceleration are used to stand for displacement, velocity, and acceleration in direction 2. The physical and mechanical parameters for the cohesive material and the linear elastic material are presented in Table 1, which correspond to those of a rock-like material.

Figure 8 Dimensions of the plate (a), boundary and loading conditions (b)

Table 1 Material properties

Using the selected parameters, the following values can be computed:

- The strain energy available for release is:

$$E_S = \frac{R_T^2 L}{2E} W = \frac{(2.6 \times 10^6)^2 \times 1}{2 \times 30 \times 10^9} \times 0.2 = 22.5 \text{ J} \quad (14)$$

- The energy loss due to fracture is:

$$E_F = G_{IC} \times W = 25 \times 0.2 = 5 \text{ J} \quad (15)$$

From equations (14) and (15), the factor  $\alpha$  is:

$$\alpha = \frac{E_S}{E_F} = \frac{22.5}{5} = 4.5 \quad (16)$$

Since  $\alpha$  is larger than 1, elastic waves are expected to be induced after damage to the cohesive layer has occurred.

### 5.1.2 Simulation results

Figure 9 shows a contour plot of the normal stress  $S_{22}$  in direction 2 for the period from the beginning of the damage to the cohesive layer. Here, one period is defined as the time it takes for the induced elastic waves to travel from the top edge of the plate to the bottom edge and to travel back to the top edge after reflection off the bottom edge.

The damage to the cohesive layer begins at approximately 8 ms when the tensile stress is equal to the tensile strength (Figure 9a). Then, the stress in the region near the cohesive layer begins to decrease (Figure 9b). The stress decrease propagates toward the bottom of the plate as stress waves. Once the stress waves reach the bottom edge (Figure 9c), they are reflected back (Figure 9d) and propagate toward the top edge (Figure 9e, f). It can also be seen that the sign of the stress changes from positive to negative as the stress waves are reflected off the bottom edge (Figure 9d, e). The distribution of stress  $S_{22}$  along the length of the plate, at different times, is presented in Figure 10. The propagation of the stress decrease and the reflection of the stress waves are clearly observed.

Figure 9 Normal stress  $S_{22}$  in direction 2 during one period after damage to the cohesive layer starts.

The damage begins at time  $t = 8$  ms

Figure 10 Stress  $S_{22}$  along the length of the plate at different times corresponding to those of Figure 9. The damage begins at time  $t = 8$  ms. The top and bottom edges of the plate are located at  $y = 0$  and  $y = 1$ , respectively

The computed time evolution of displacement and velocity of the top point A (see Figure 8) is presented in Figure 11. It can be seen that the displacement increases linearly at first, and then starts to decrease as the cohesive layer is damaged. But instead of decreasing to zero, it oscillates around the zero-position.

A similar evolution pattern is observed for the velocity: the velocity is relatively small before damage to the cohesive layer starts; it increases once the cohesive damage occurs and oscillates afterward. The maximum velocity of the point A is 0.32 m/s, which is 35.5 times the applied displacement rate. Both the displacement and the velocity oscillate with the same period of approximately 1.6 ms.

The time evolution of different types of energy (strain energy, kinetic energy and fracture energy) is presented in Figure 12. It is noted that the strain energy increases at first and then starts to decrease when cohesive damage occurs. While the kinetic energy remains close to zero before the cohesive damage, it starts to increase when cohesive damage occurs. The fact that the kinetic energy is close to zero before the onset of cohesive damage ensures that the relatively high applied displacement rate used in the simulation has a negligible effect on the solution. After the cohesive damage starts, both the strain energy and the kinetic energy oscillate harmonically with the same period of approximately 0.8 ms. These two types of energy are also converted back and forth into each other: when the kinetic is zero the strain energy is largest and vice versa. The maximum value of the kinetic energy after damage to the cohesive material is approximately 17.5 J. The energy dissipated due to the damage of the cohesive layer, i.e., the fracture energy, increases suddenly from 0 to 5 J upon damage of the cohesive layer. This value of fracture energy is equal to the value predicted by the analytical model, equation (15).

It is worth noting that the oscillation period of the displacement and the velocity ( $T = 1.6$  ms) is double that of the kinetic and strain energies ( $T = 0.8$  ms). Figure 13 illustrates this observation more clearly. This result was obtained for the discrete spring-mass model and is again obtained for this continuum model.

Figure 11 Time evolution of displacement and velocity of the point A

Figure 12 Time evolution of different types of energy of the whole model

Figure 13 Time evolution of the kinetic energy and the displacement showing that the oscillation period of the displacement is double that of the kinetic energy

## 5.2 Influence of the applied displacement rate

To demonstrate that an increase in the applied displacement rate has a negligible effect on the final results, the simulation was re-run with a displacement rate of 0.9 mm/s, which is ten times smaller than in the previous case.

The simulation results are presented in Figure 14 for the time evolution of displacement and velocity of the point A, and in Figure 15 for the time evolution of different types of energy. The damage of the cohesive material occurs at around 77 ms. After that, identical trends in the damage evolution, as seen in the previous case, were obtained. For instance, after damage to the cohesive material, the displacement and the velocity of the point A and kinetic and strain energies oscillate. The oscillation period of the kinetic and strain energies is approximately 0.8 s (Figure 15b), while the displacement and velocity of the point A oscillate with a period of approximately 1.6 s (Figure 14b). These periods are identical to those obtained in the previous case. The maximum velocity of the point A is 0.32 m/s and the maximum kinetic energy is 17.5 J, which again are both identical to those obtained in the previous case. Thus, the simulation shows that the reduced applied displacement rate only expands the elastic deformation phase and delays the damage to the cohesive layer. After the cohesive layer is damaged, the behavior of the model is identical to the previous case.

Figure 14 Time evolution of the displacement and the velocity of point A: (a) from the beginning, (b) a zoom-in during and after damage to the cohesive layer

Figure 15 Time evolution of different types of energy of the whole model: (a) from the beginning, (b) a zoom-in during and after damage to the cohesive layer

### 5.3 Influence of tensile strength on the amplitude of induced elastic waves

In this section we investigate the influence of the factor  $\alpha$  on the amplitude of the induced elastic waves, which is reflected by the maximum velocity of the point A. The expression for  $\alpha$ , as presented in equation (12), is repeated here for convenience:

$$\alpha = \frac{R_T^2 L}{2G_{IC} E}$$

As is seen in the above expression,  $\alpha$  can vary by changing either the tensile strength  $R_T$ , the length of the specimen  $L$ , the fracture toughness  $G_{IC}$ , or the Young's modulus  $E$ . In the following only a change in the tensile strength is considered. The change in tensile strength for a Mode I fracture is equivalent to a change in shear strength for a Mode II fracture. Thus, conclusions obtained in this simulation are also valid for the Mode II fracture.

Five cases with different values of tensile strength are considered (Table 5.2). Since the applied displacement rate has been proven to have a negligible effect on the mechanical response of the system, a displacement rate of 9 mm/s is used. For all of these five cases the loading rate is applied within 20 ms.

Table 5.2 Analysis cases for studying the influence of  $\alpha$

#### 5.3.1 Simulation results

The time evolution of the displacement and the velocity of the point A are presented in Figure 16 and Figure 17, respectively. As seen in Figure 16, for case 1 ( $\alpha = 0.24$ ), the velocity of the point A is virtually zero for the entire time, before and after damage to the cohesive material. The predicted value of the velocity of the point A after the damage of the cohesive material is given by equation 13:

$$\dot{u}_A = \frac{1}{1-\alpha} \dot{u} = \frac{1}{1-0.24} \times 9 = 11.8 \text{ mm/s}$$

This velocity is of the same magnitude as the applied displacement rate (9 mm/s).

Then, the factor  $\alpha$  is varied from 2.4 in case 2 to 14.1 in case 5. This corresponds to a range of tensile strength lying between 1.9 MPa and 4.6 MPa. As  $\alpha$  increases, the time at which damage to the cohesive material occurs (which corresponds to when the velocity of the point A changes significantly) is expectedly to be delayed (Figure 16). The dynamic behavior of the system after the cohesive damage has occurred is reflected by the time evolution of the displacement at point A (Figure 17). For all cases: the velocity of the point A oscillates with a similar period of approximately 1.6 ms. However, as  $\alpha$  is increased from 2.4 to 14.1, the maximum velocity of the point A increases from 0.19 m/s (21 times the applied displacement rate) to 0.99 m/s (111 times the applied displacement rate).

Figure 16 Time evolution of the velocity in direction 2 of the point A for 5 cases

Figure 17 Time evolution of the displacement in direction 2 of the point A for 5 cases

The maximum velocity of the point A is plotted in Figure 18a as a function of the coefficient  $\alpha$ . An increasing linear relationship between these two quantities, which is represented by a straight line passing through the origin, is observed. Figure 18b shows the maximum velocity as a function of the tensile strength. Again, it is noted that the maximum velocity tends to zero for small tensile strength and increases rapidly as the tensile strength increases.

The above observations are consistent with the conclusion on the role of the ratio between the strain energy release and the fracture energy, which is represented through the coefficient  $\alpha$ . It is stated that as the ratio between the strain energy release and the fracture energy increases the intensity of the induced elastic waves will also increase.

This conclusion can be extrapolated to a Mode II fracture (shear-mode). Therefore, when the shear strength of the fracture increases, the intensity of the elastic waves, that are induced when the fracture slips, increases too. For a Mode II fracture and for a given stress state, the shear strength of the fracture is solely proportional to the friction coefficient of the fracture. In other words, if the friction coefficient of the fracture can be reduced, which will lead to a

reduction of the shear strength of the fracture, and the intensity of the induced elastic waves will be reduced (Ngo et al., 2019).

Figure 18 Maximum velocity of the point A as function of (a) coefficient  $\alpha$  and (b) tensile strength

## 6 Conclusions

In this paper it has been shown how brittle failure resulting from fracturing processes, produces dynamic response that induces elastic wave generation responsible for acoustic events or micro-seismicity.

A simple one-dimensional analytical model that respects the law of conservation of energy allows us to illustrate the oscillations of the system after failure. It is shown that the energy of elastic deformation is converted into kinetic energy that allows the elastic waves to propagate within the system.

A Dynamic Finite Element Analysis was carried out to determine the parameters that influence the amplitudes and the velocities of the waves generated by the fracture rupture. The numerical results indicate that the opening velocity of the fracture depends on a factor  $\alpha$ , which represents the ratio of the elastic strain energy available in the system to the energy consumed by the development of the fracture. It is shown that elastic wave generation occurs when the factor  $\alpha$  is greater than 1

Since this factor is calculated from the tensile strength and the toughness of the fracture as well as the Young's modulus of the material, a parametric study was run. It was found that elastic wave velocities do not depend on the rate of loading but are strongly dependent on the tensile strength of the material. Indeed, the higher the factor  $\alpha$  is, the larger will be the wave amplification.

In a rock engineering context, these conclusions might be of interest in, for instance, determining the risk of inducing micro-seismicity triggered by underground work or geothermal energy extraction.

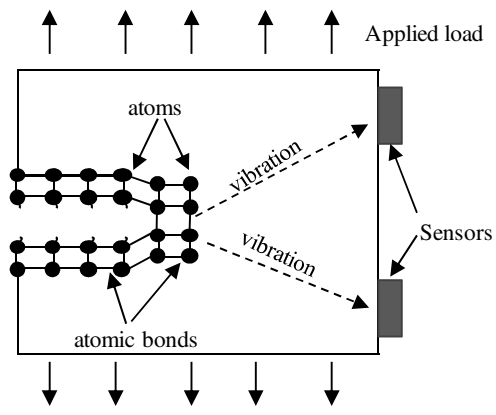
## Acknowledgements

The authors wish to thank the Dassault Systèmes Foundation for supporting this research.

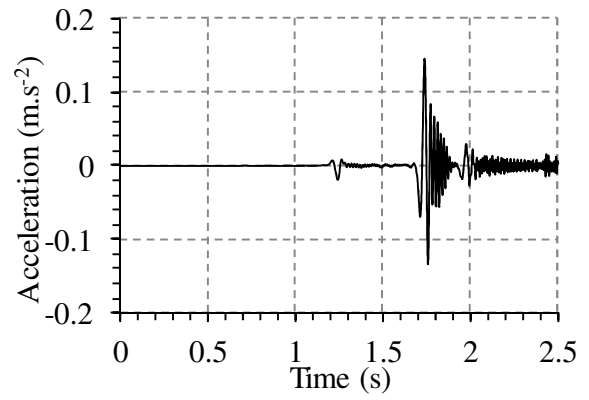
## References

- Abaqus, 2016. Analysis User's Manual Version R2016, Dassault Systèmes.
- Boudet, J., Ciliberto, S., Steinberg, V., 1995. Experimental study of the instability of crack propagation in brittle materials. *EPL (Europhysics Letters)* 30, 337.
- Bratov, V., Petrov, Y., 2007. Application of incubation time approach to simulate dynamic crack propagation, *International Journal of Fracture* 146, 1-2, 53-60.
- Cundall, P.A., Hart, R.D., 1992. Numerical modelling of discontinua. *Engineering Computations* 9, 101-113.
- Evans, A., Linzer, M., 1977. Acoustic emission in brittle materials. *Annual Review of Materials Science* 7, 179-208.
- Fineberg, J., Gross, S.P., Marder, M., Swinney, H.L., 1992. Instability in the propagation of fast cracks. *Physical Review B* 45, 5146.
- Gutenberg, B., Richter, C.F., 1956. Earthquake magnitude, intensity, energy, and acceleration: (Second paper). *Bulletin of the Seismological Society of America* 46, 105-145.
- Hardy Jr, H.R., 2003. *Acoustic emission/microseismic activity: volume 1: principles, techniques and geotechnical applications*. CRC Press.
- Hazzard, J., Young, R., 2000. Simulating acoustic emissions in bonded-particle models of rock. *International Journal of Rock Mechanics and Mining Sciences* 37, 867-872.
- Hazzard, J., Young, R., 2004. Dynamic modelling of induced seismicity. *International Journal of Rock Mechanics and Mining Sciences* 41, 1365-1376.
- Kaiser, P., Tang, C., 1998. Numerical simulation of damage accumulation and seismic energy release during brittle rock failure—Part II: Rib pillar collapse. *International Journal of Rock Mechanics and Mining Sciences* 35, 123-134.
- Kanamori, H., 1977. The energy release in great earthquakes. *Journal of Geophysical Research (1896-1977)* 82, 2981-2987.
- Keshavarz, M., Pellet, F., Rousseau, C., Hosseini, K.A., 2008. Comparing the results of acoustic emission monitoring in Brazilian and uniaxial compression tests, *ISRM International Symposium-5th Asian Rock Mechanics Symposium*. International Society for Rock Mechanics.
- Lisjak, A., Liu, Q., Zhao, Q., Mahabadi, O., Grasselli, G., 2013. Numerical simulation of acoustic emission in brittle rocks by two-dimensional finite-discrete element analysis. *Geophysical Journal International* 195, 423-443.
- Lockner, D., 1993. The role of acoustic emission in the study of rock fracture. *International Journal of Rock Mechanics and Mining Sciences & Geomechanics Abstracts* 30, 883-899.

- Moradian, Z., Einstein, H.H., Ballivy, G., 2016. Detection of cracking levels in brittle rocks by parametric analysis of the acoustic emission signals. *Rock Mechanics and Rock Engineering* 49, 785-800.
- Munjiza, A.A., 2004. *The combined finite-discrete element method*. John Wiley & Sons.
- Ngo, D.T., Pellet, F.L., Bruel, D. (2017), Modeling of dynamic crack propagation under quasi-static loading, *Proc. 15th International Conference of the International Association of Computer Methods and Advances in Geomechanics, IACMAG, Wuhan, China*.
- Ngo, D.T., Pellet, F.L., Bruel, D., 2019, Modeling of fault slip during hydraulic stimulation in naturally fractured medium, *Geomechanics and Geophysics for Geo-Energy and Geo-Resources*, Vol 5, 3: 237–251, ([doi.org/10.1007/s40948-019-00108-1](https://doi.org/10.1007/s40948-019-00108-1)).
- Ohnaka, M., Mogi, K., 1982. Frequency characteristics of acoustic emissions in rocks under uniaxial compression and its relation to the fracturing process to failure. *Journal of Geophysical Research*, 87(B5): 3873 - 3884.
- Pellet, F.L., Selvadurai, A.P.S. (2016), Rock damage mechanics, Chapter 3, In *Rock Mechanics and Engineering: Vol. 1 Principles*, ISRM Book series, CRC Press / Balkema – Taylor & Francis Group, Leiden, pp 65-107.
- Petrov, Y.V., 2007. On the incubation stage of fracture and structural transformations in continuous media under pulse energy injection. *Journal Mechanics of Solids* 42, 5, 692-699.
- Petrov, Y., Kazarinov, N., Bratov, V., 2016. Dynamic crack propagation: quasistatic and impact loading. *Procedia Structural Integrity* 2, 389-394.
- Pollock, A.A., 1973. Acoustic emission - 2: Acoustic emission amplitudes. *Non-Destructive Testing* 6, 264-269.
- Potyondy, D.O., Cundall, P.A., 2004. A bonded-particle model for rock. *International Journal of Rock Mechanics and Mining Sciences* 41, 1329-1364.
- Scholz, C., 1968a. Experimental study of the fracturing process in brittle rock. *Journal of Geophysical Research* 73, 1447-1454.
- Ravi-Chandar, K., 2004. *Dynamic fracture*, Elsevier
- Rosakis, A.J., Ravichandran, G.T., 2000. Dynamic failure mechanics. *International Journal of Solids and Structures* 37, 1–2, 331-348.
- Scholz, C., 1968b. The frequency-magnitude relation of microfracturing in rock and its relation to earthquakes. *Bulletin of the Seismological Society of America* 58, 399-415.
- Swindlehurst, W., 1973. Acoustic emission - 1 Introduction. *Non-Destructive Testing* 6, 152-158.
- Tang, C., 1997. Numerical simulation of progressive rock failure and associated seismicity. *International Journal of Rock Mechanics and Mining Sciences* 34, 249-261.
- Tang, C.A., Kaiser, P.K., 1998. Numerical simulation of cumulative damage and seismic energy release during brittle rock failure—Part I: Fundamentals. *International Journal of Rock Mechanics and Mining Sciences* 35, 113-121.

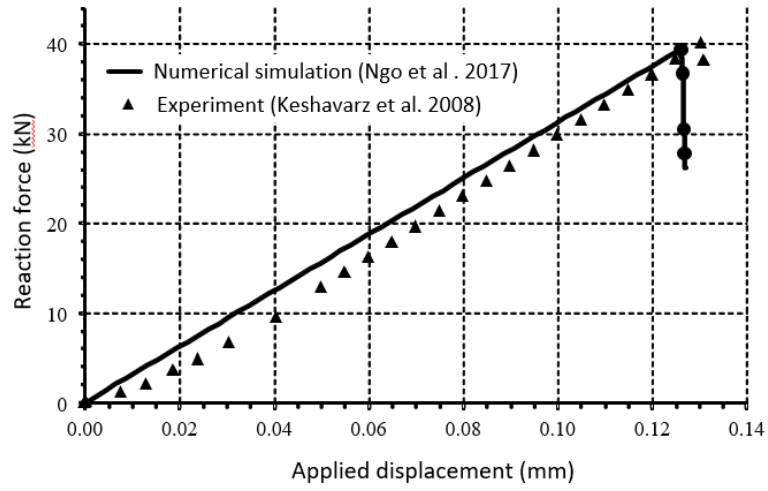


(a)

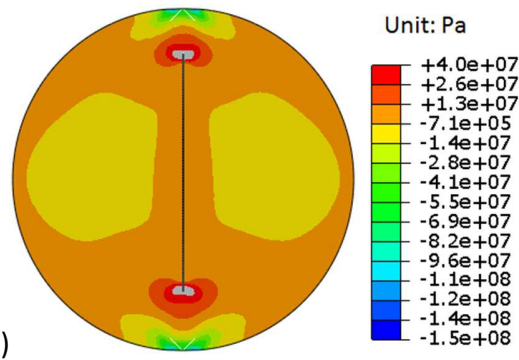


(b)

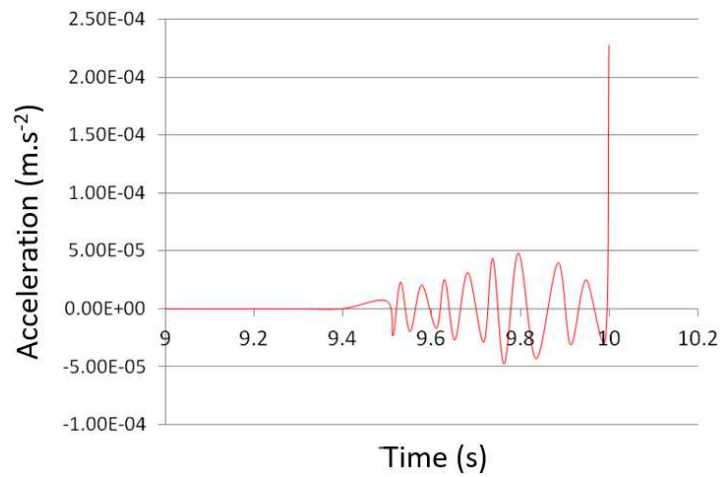
Figure 1. (a) Illustration of generation of elastic waves from fracture propagation, (b) Example of signals recorded by AE/MS sensors (e.g., acceleration)



a)



b)



c)

Figure 2. Numerical simulation of a Brazilian test (Ngo et al. 2017); a- load-displacement curve; b- fracture propagation and stress redistribution, c- acceleration versus time in point M

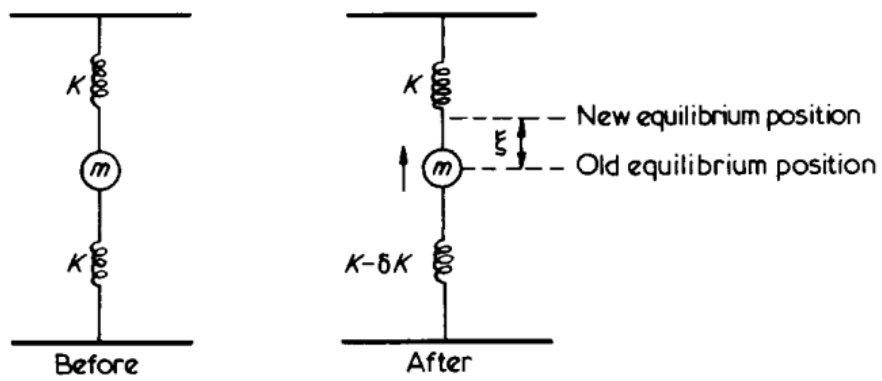


Figure 3. A spring-mass model after Pollock (1973)

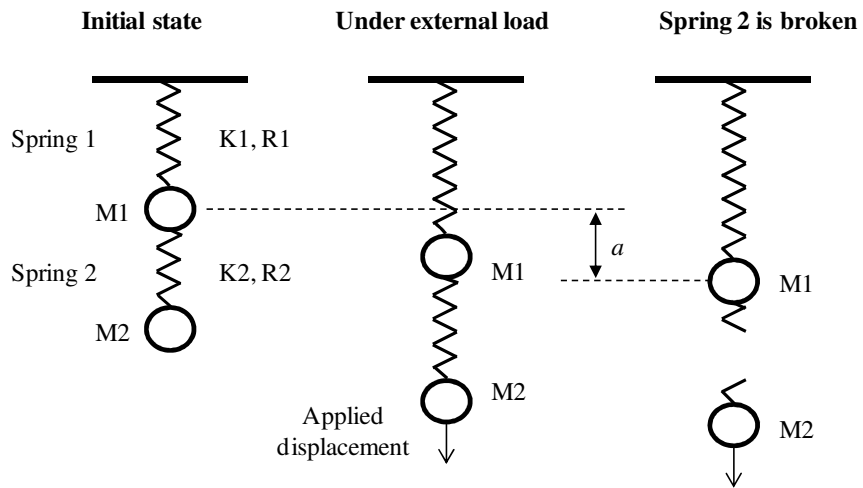


Figure 4. Proposed spring-mass model:  $K_1$  and  $R_1$  are stiffness and strength of the spring 1,  $K_2$  and  $R_2$  are stiffness and strength of the spring 2

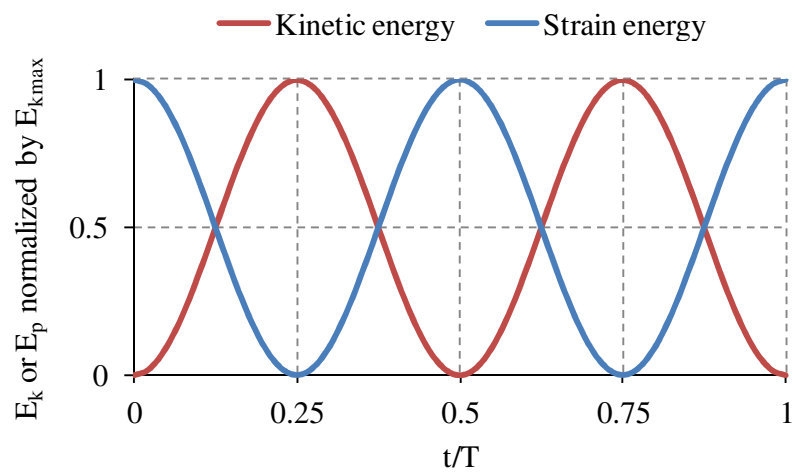


Figure 5. Time evolution of kinetic energy and strain energy; T is the period of the vibration of the mass

M1

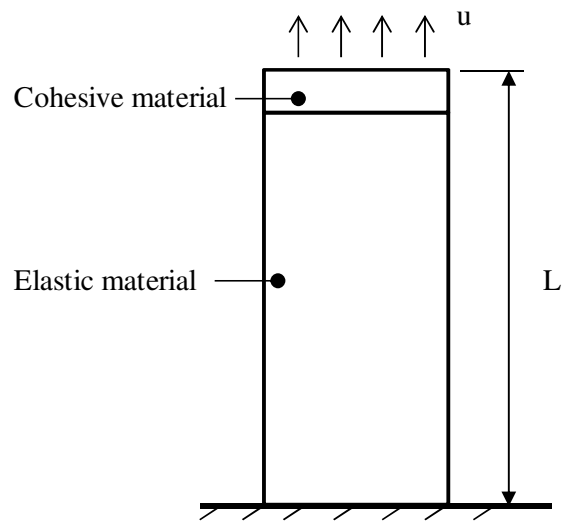


Figure 6. Plate model made of two materials. The cohesive layer has zero thickness.

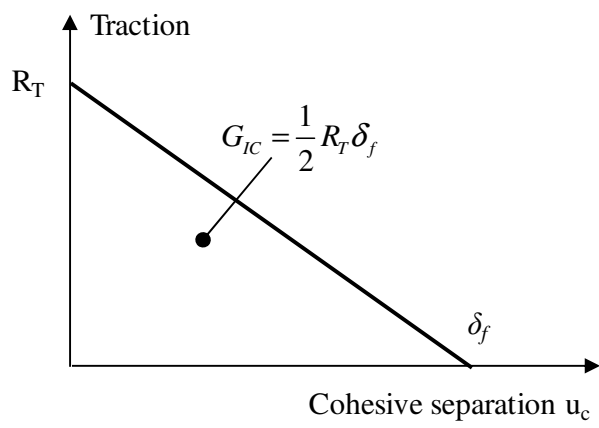


Figure 7. Cohesive traction-separation law

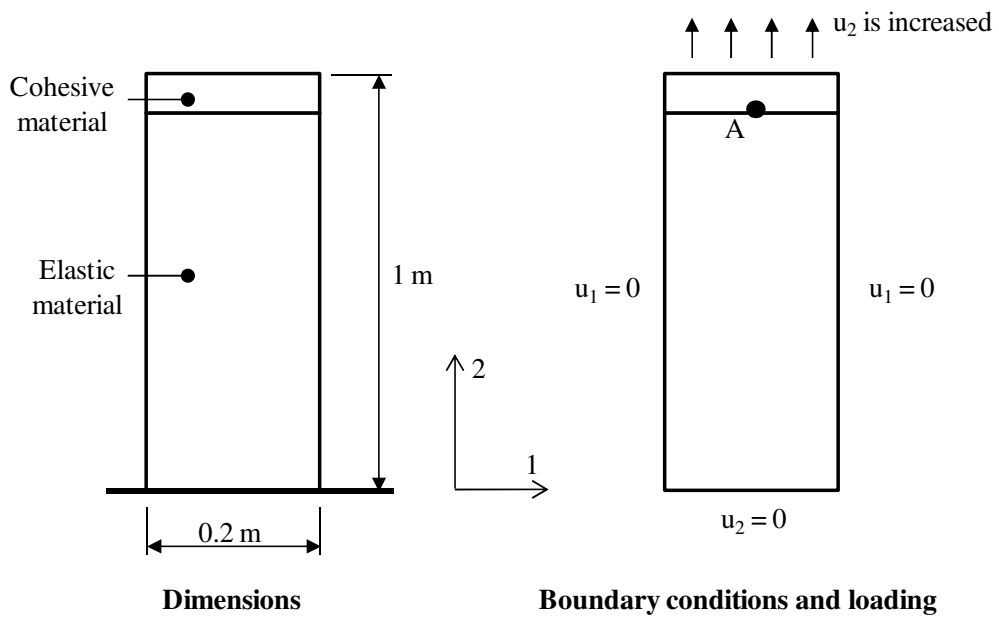


Figure 8. Dimensions of the plate (a), boundary and loading conditions (b)

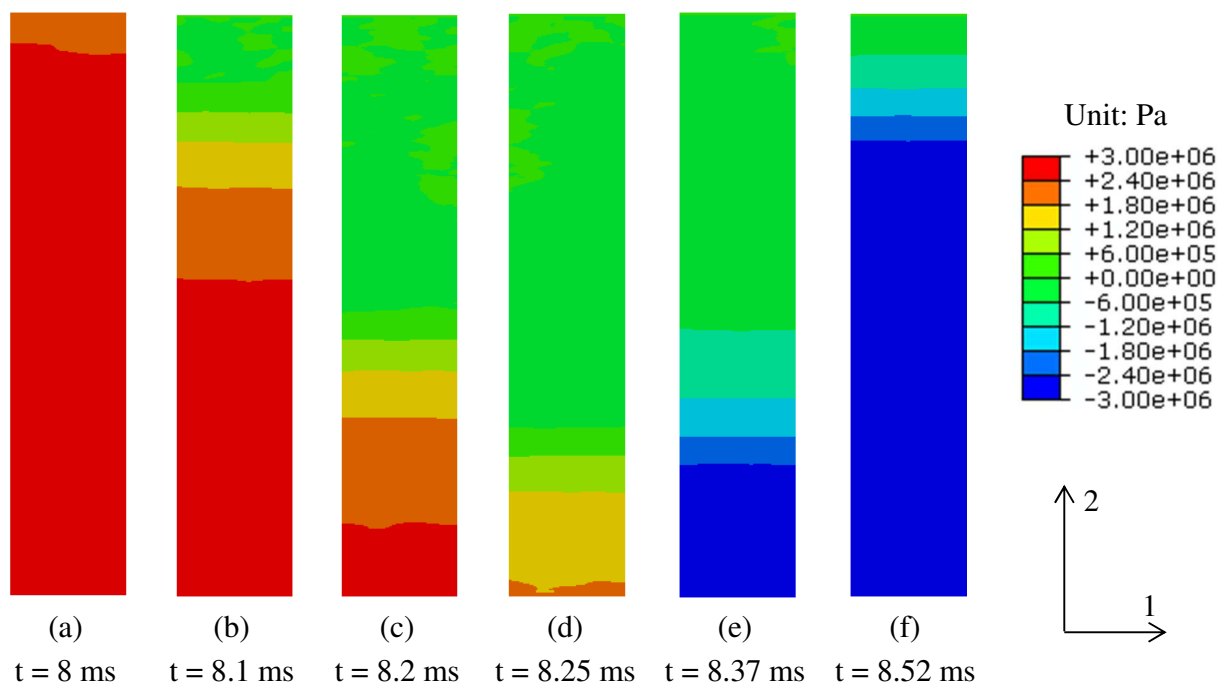


Figure 9. Normal stress S22 in direction 2 during one period since the damage of the cohesive layer starts. The damage begins at time  $t = 8$  ms

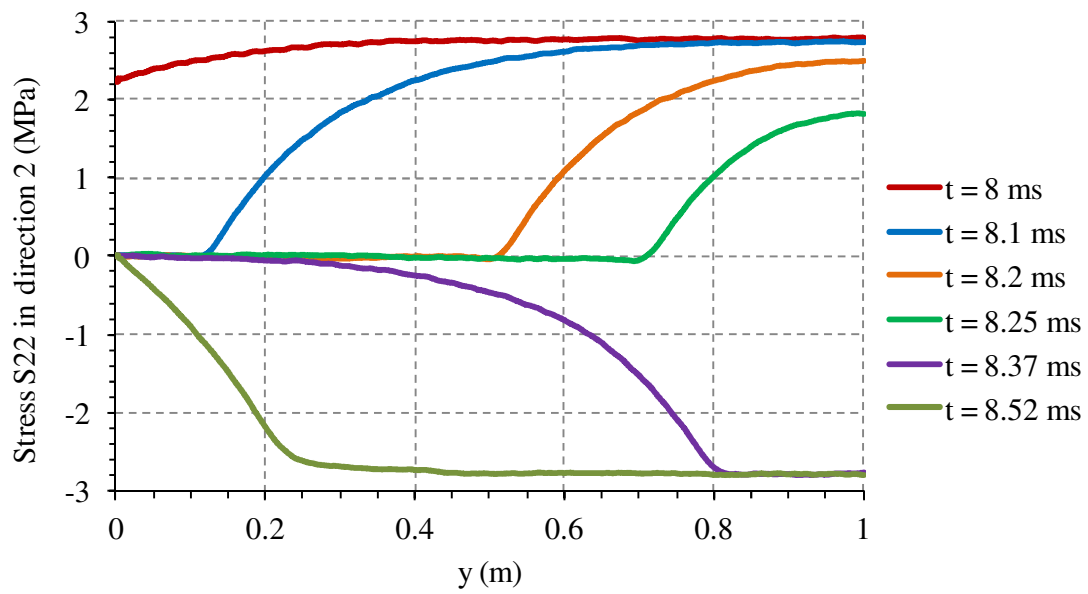


Figure 10. Stress S22 along the length of the plate at different times corresponding to those of Figure . The damage begins at time  $t = 8$  ms. The top and bottom edges of the plate are located at  $y = 0$  and  $y = 1$ , respectively.

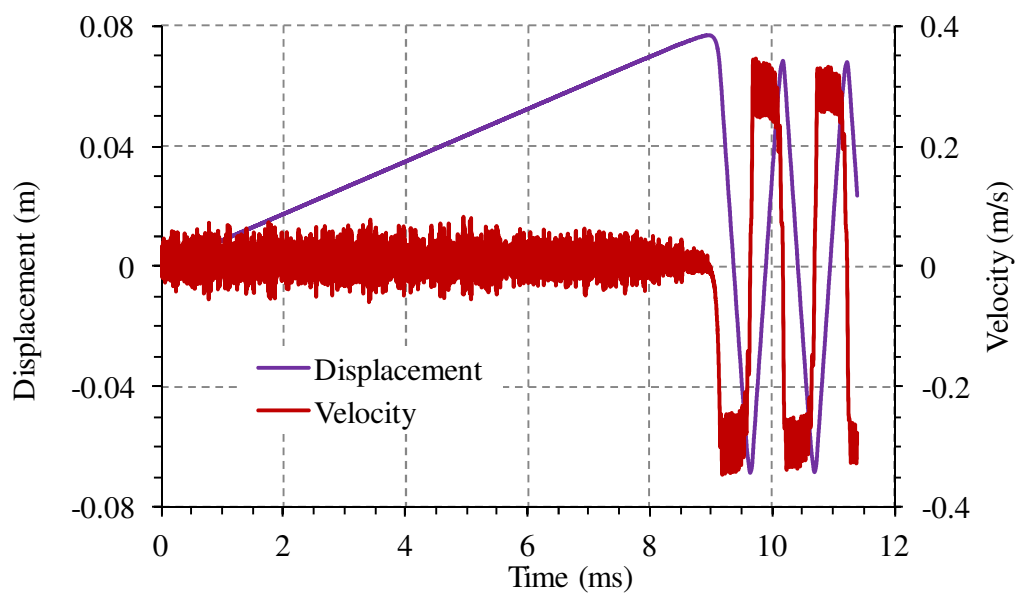


Figure 11. Time evolution of displacement and velocity of the point A

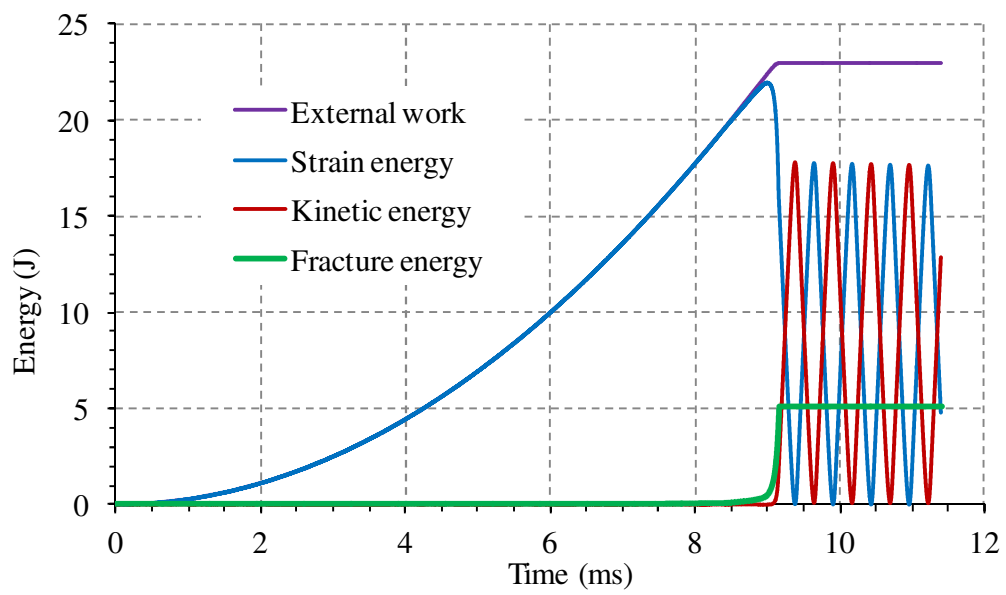


Figure 12. Time evolution of different types of energy of the whole model

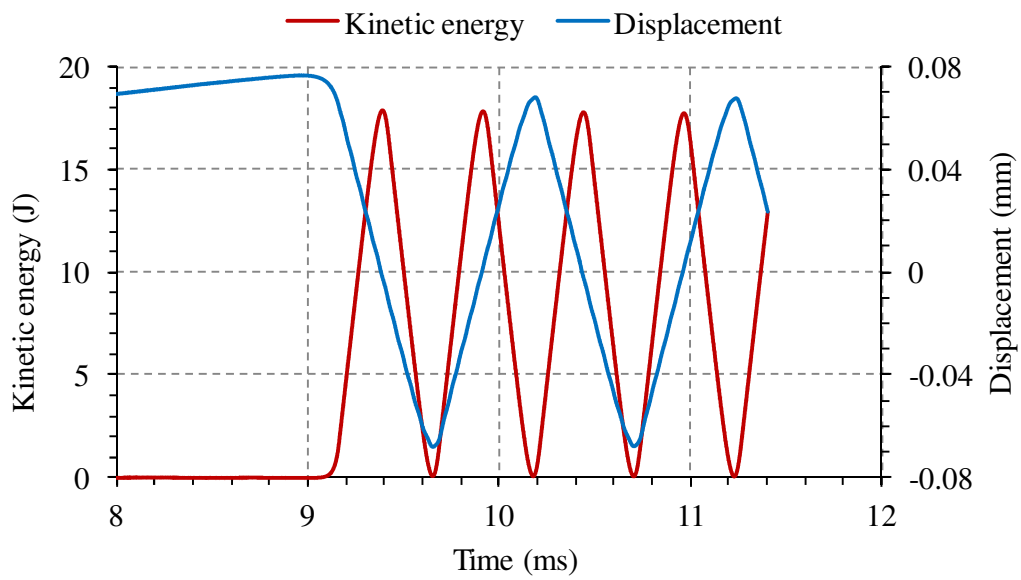
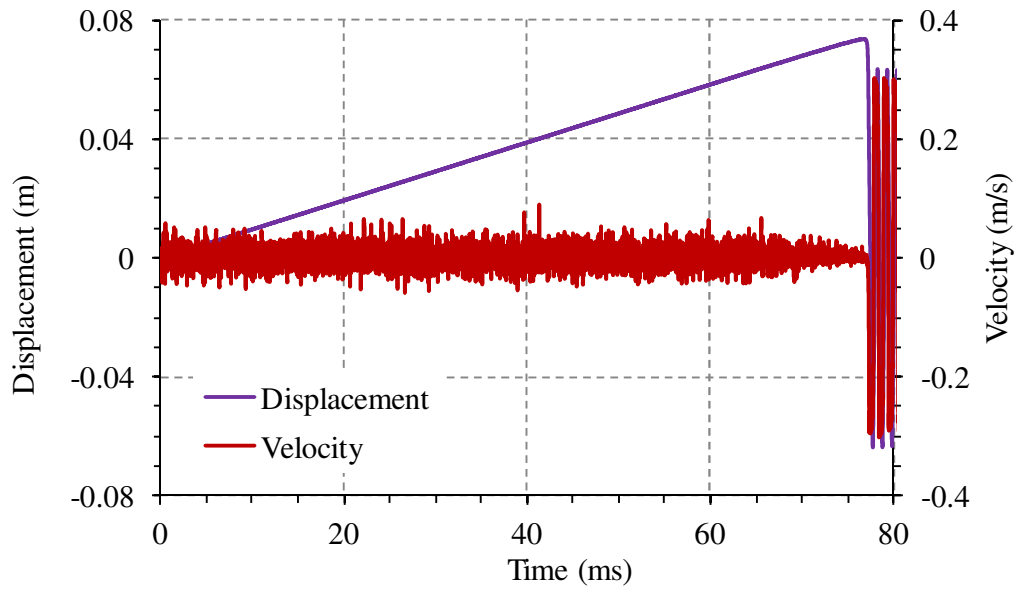
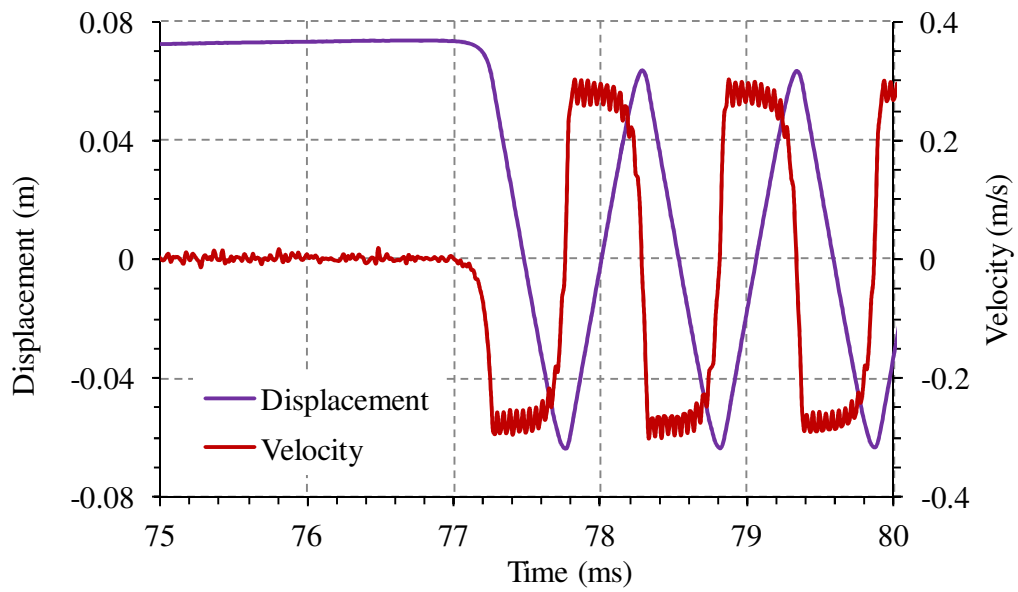


Figure 13. Time evolution of the kinetic energy and the displacement showing that oscillation period of the displacement is double that of the kinetic energy

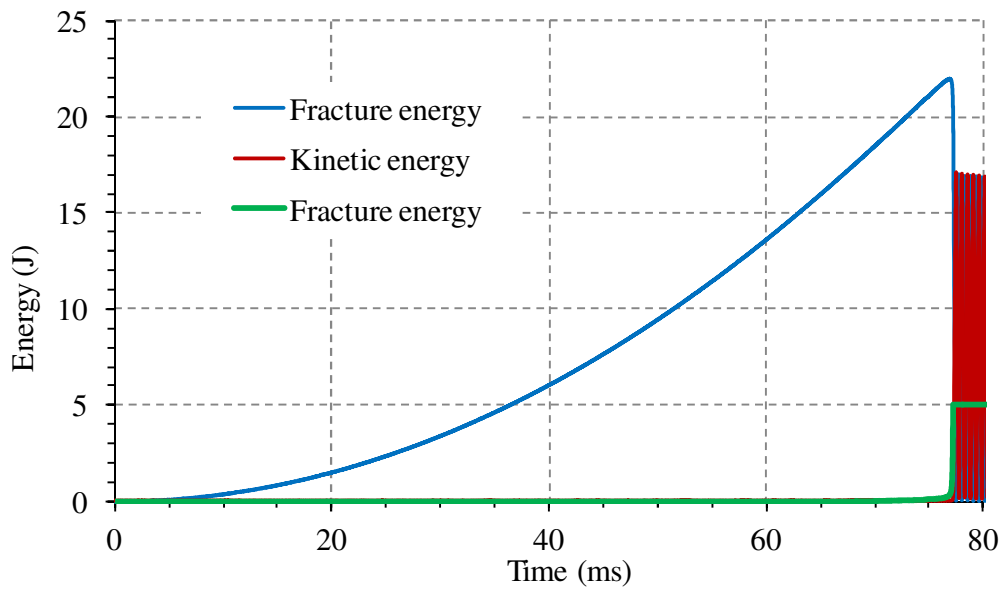


(a)

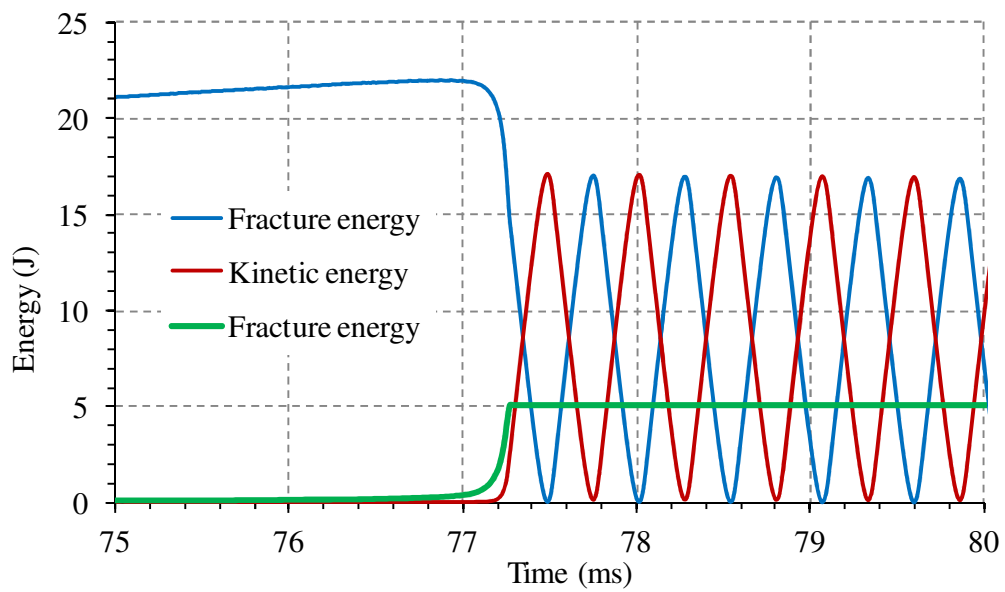


(b)

Figure 14. Time evolution of the displacement and the velocity of point A: (a) from the beginning, (b) a zoom-in during and after the damage of the cohesive layer



(a)



(b)

Figure 15. Time evolution of different types of energy of the whole model: (a) from the beginning, (b) a zoom-in during and after the damage of the cohesive layer

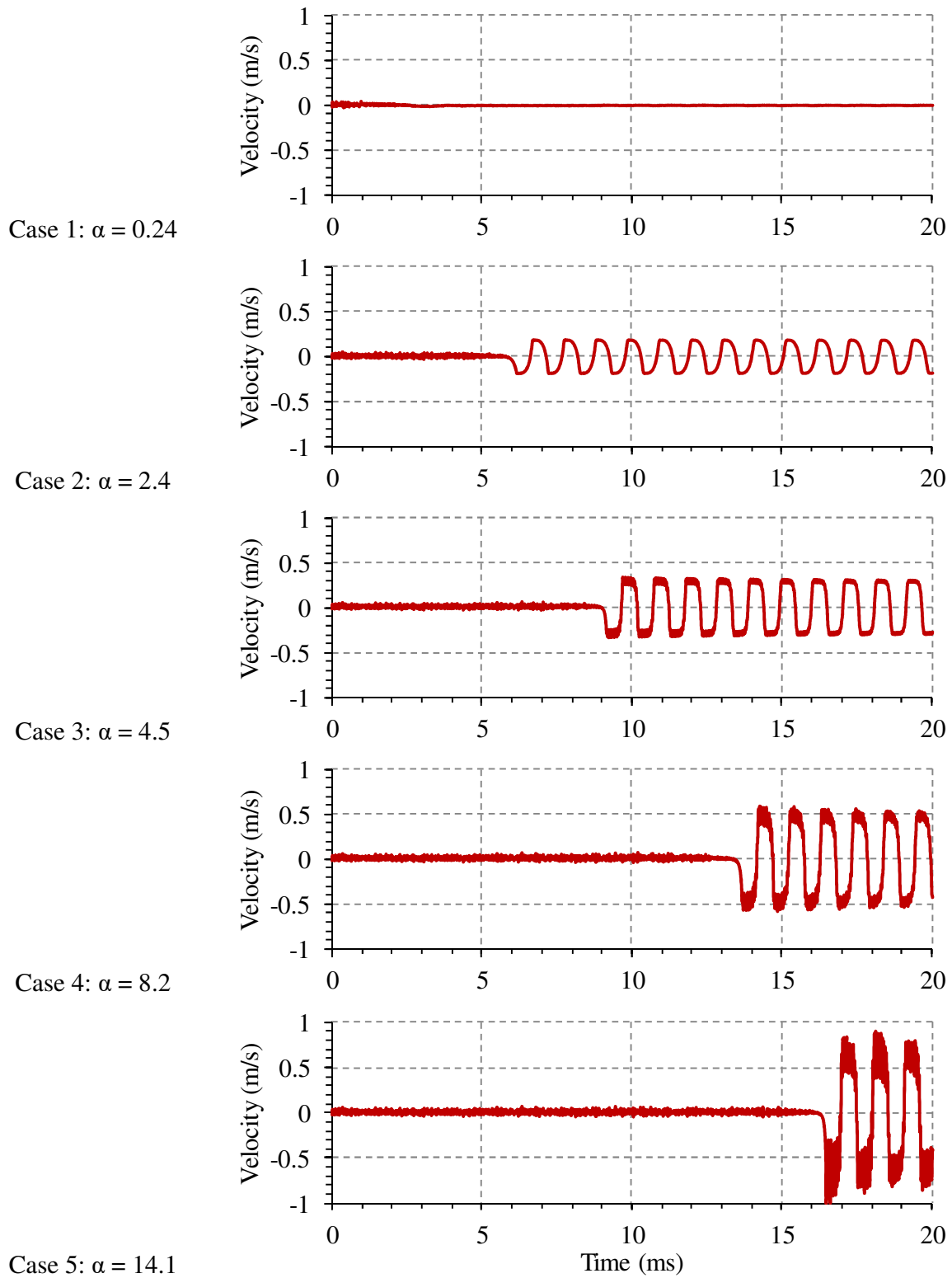


Figure 16. Time evolution of the velocity in direction 2 of the point A for 5 cases

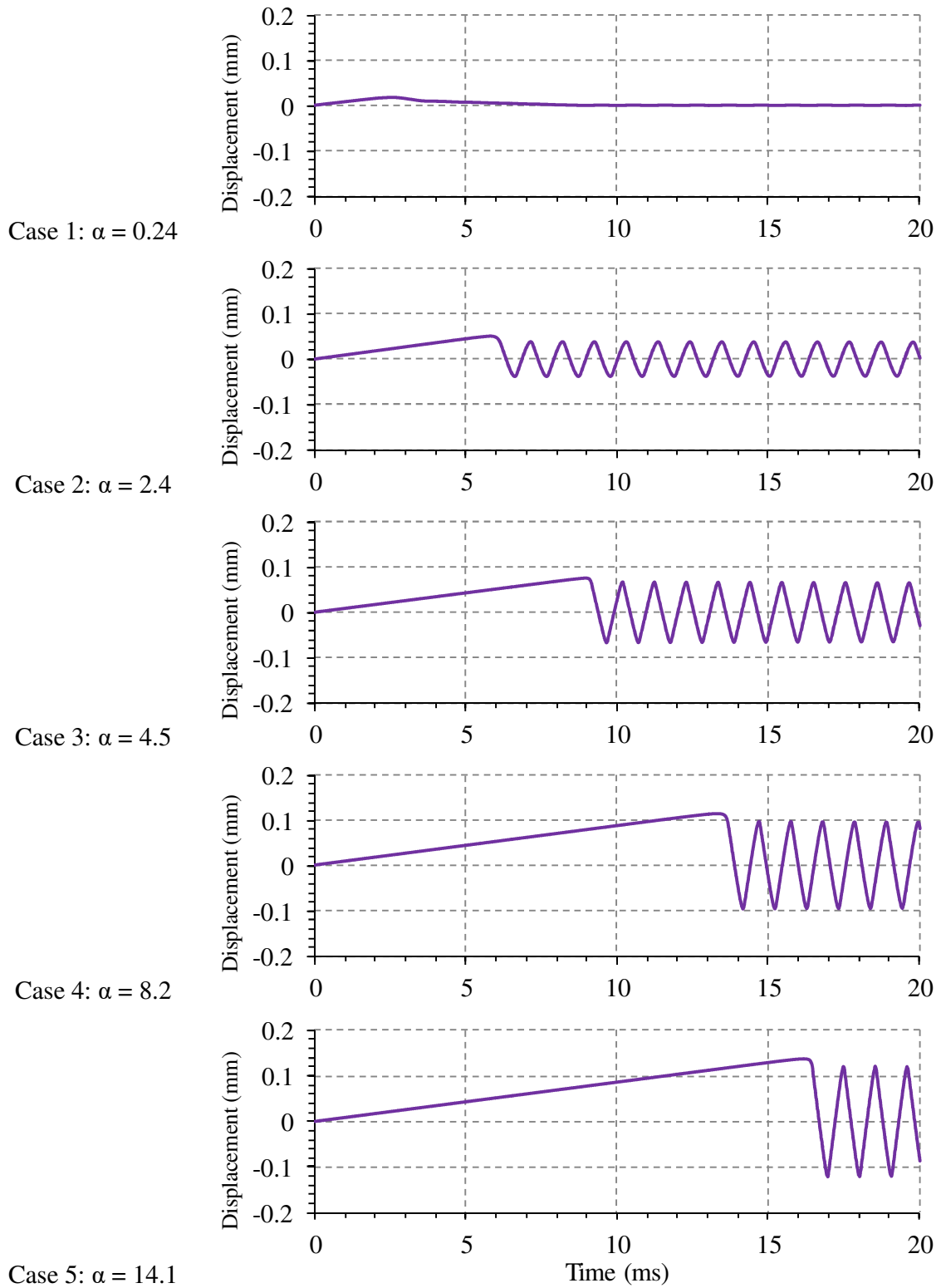
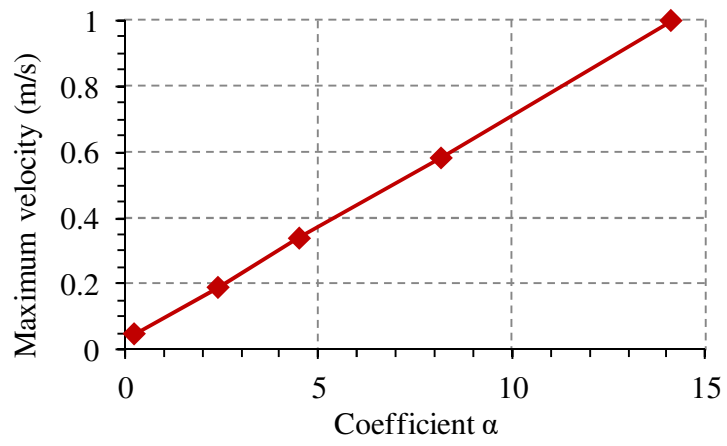
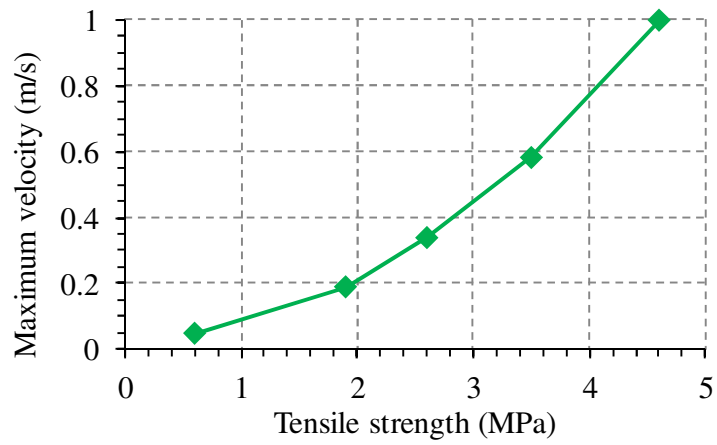


Figure 17. Time evolution of the displacement in direction 2 of the point A for 5 cases



(a)



(b)

Figure 18. Maximum velocity of the point A as function of (a) coefficient  $\alpha$  and (b) tensile strength

Table 1 Material properties

Property	Value
<b>Cohesive material</b>	
Tensile strength	$R_T = 2.6 \text{ MPa}$
Fracture toughness	$G_{IC} = 25 \text{ J/m}^2$
<b>Linear elastic material</b>	
Young's modulus	$E = 30 \text{ GPa}$
Poisson's ratio	0.22
Density	$\rho = 2500 \text{ kg/m}^3$
P-wave speed	$C_p = 3464 \text{ m/s}$

Table Error! No text of specified style in document..2 Analysis cases for studying influence of  $\alpha$

Case	Tensile strength $R_T$ (MPa)	$\alpha$
1	0.6	0.24
2	1.9	2.4
3	2.6	4.5 (studied in subsection 5.1)
4	3.5	8.2
5	4.6	14.1